AGU PUBLICATIONS

Geophysical Research Letters

RESEARCH LETTER
10.1002/2016GL071840

Key Points:
- The mid-lithospheric discontinuity beneath the western and central North China Craton occurs between 80 and 120 km depth
- Stacked teleseismic autocorrelograms reveal fine-scale lithospheric structure with high-frequency seismic waves
- The mid-lithosphere discontinuity agrees well with the base of the thermal lithosphere

Supporting Information:
- Supporting Information S1

Correspondence to:
W. Sun,
swj@mail.iggcas.ac.cn

Citation:
Sun, W., and B. L. N. Kennett (2017), Mid-lithosphere discontinuities beneath the western and central North China Craton, *Geophys. Res. Lett.*, *44*, 1302–1310, doi:10.1002/2016GL071840.

Received 4 NOV 2016
Accepted 26 JAN 2017
Accepted article online 30 JAN 2017
Published online 13 FEB 2017

Mid-lithosphere discontinuities beneath the western and central North China Craton

Weijia Sun[1] **and B. L. N. Kennett**[2]

[1]Key Laboratory of Earth and Planetary Physics, Institute of Geology and Geophysics, Chinese Academy of Sciences, Beijing, China, [2]Research School of Earth Sciences, Australian National University, Canberra, ACT, Australia

Abstract By analyzing *P* reflectivity extracted from stacked autocorrelograms for teleseismic events on a dense seismic profile, we obtain a detailed image of the mid-lithosphere discontinuity (MLD) beneath western and central North China Craton (NCC). This seismic daylight imaging exploits a broad high-frequency band (0.5–4 Hz) to reveal the fine-scale component of multi-scale lithospheric heterogeneity. The depth of the MLD beneath the western and central parts of the NCC ranges 80–120 km, with a good match to the transition to negative *S* velocity gradient with depth from Rayleigh wave tomography. The MLD inferred from seismic daylight imaging also has good correspondence with the transition from conductive to convective regimes estimated from heat flow data indicating likely thermal control within the seismological lithosphere.

1. Introduction

In recent years there have been widespread reports of an *S* velocity reduction at depths around 80–120 km inferred from the interpretation of *Sp* receiver functions associated with the presence of negative *Sp* phases [e.g., *Abt et al.*, 2010; *Chen et al.*, 2014; *Ford et al.*, 2010; *Tharimena et al.*, 2016]. In tectonically active areas with thin lithosphere, this discontinuity has been interpreted as the lithosphere-asthenosphere boundary (LAB). But beneath stable geologic units like cratons with thick and cold lithosphere the identification has been made with a mid-lithosphere discontinuity (MLD) [e.g., *Abt et al.*, 2010; *Chen et al.*, 2014; *Selway et al.*, 2015]. Discontinuities have been suggested at a variety of depths beneath cratons, with the deepest MLD at about 200 km depth proposed for station FRB in North America Craton where the LAB is at about 240 km depth [*Calò et al.*, 2016].

Receiver function studies investigate the discontinuity distribution within the Earth beneath seismic stations by using primary waves (*P* or *S*) and their conversions (*Ps* or *Sp*). To concentrate attention on major structures and reduce noise, receiver function studies concentrate on the low-frequency components of the wavefield (typically 0.03–1 Hz for *P* and 0.03–0.5 Hz for *S*). With this choice of frequency band, the vertical resolution is about 15 km, but this is still better than that which can normally be achieved with surface wave tomography.

An alternative way to explore lithospheric discontinuities is to extract reflectivity from continuous or earthquake waveforms in a higher-frequency band (0.5–4 Hz). This approach allows resolution of finer-scale lithospheric structures (~2 km in depth) [*Kennett*, 2015]. *P* reflectivity constructed from the autocorrelations of continuous waveforms has been used to image the Moho discontinuity [*Gorbatov et al.*, 2013; *Kennett et al.*, 2015] and the LAB [*Kennett*, 2015] across the Australian continent. *Sun and Kennett* [2016a] have presented the method of *seismic daylight imaging* (SDI), which exploits high signal-to-noise ratio teleseisms to explore lithospheric layering, rather than continuous seismic signals.

In this work we explore the lithospheric structures beneath the western and central North China Craton using the SDI method with a very dense linear array (see Figure 1b). The array extended west to east for about 1000 km with average station interval of about 15 km and was deployed by the Institute of Geology and Geophysics, Chinese Academy of Sciences, under North China Interior Structure Project (NCISP). The profile of 64 broadband stations crosses a range of different geological environments, from the Qilian Orogen in the west, the western North China Craton (NCC) in the central zone, and to the Trans-North China Orogen (TNCO) in the east. Each station has been used to construct lithospheric *P* wave reflectivity using the autocorrelograms of vertical component seismograms from teleseisms.

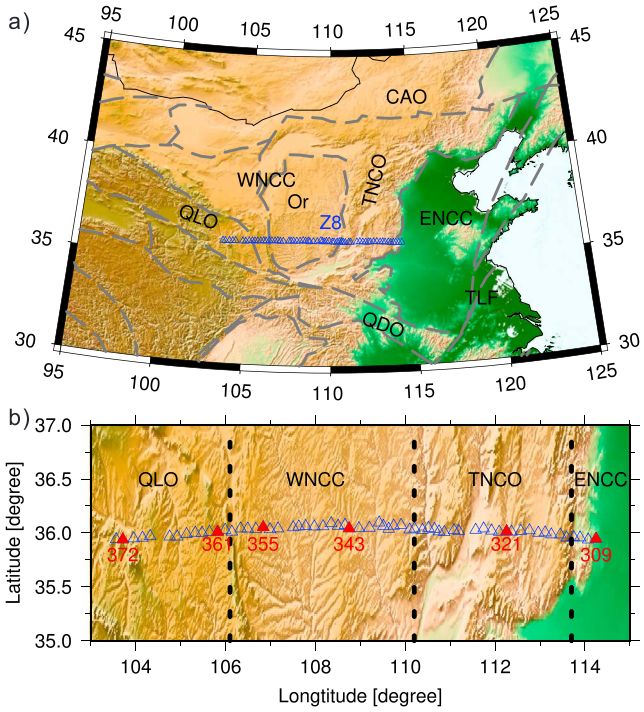

Figure 1. (a) The main tectonic units around the North China Craton (NCC) indicated by gray dashed lines. Key to marked features: CAO, Central Asian Orogen; ENCC, eastern NCC; QDO, Qinglin-Dabie Orogen; QLO, Qilian Orogen; Or, Ordos Basin; TLF, Tanlu Fault; WNCC, western NCC. The Z8 stations used in this study are displayed with blue triangles. (b) Detailed view of the station locations spanning different geological environments. The stations used in Figure 2 are marked with red solid triangles.

The two major parts of the North China Craton in the west and east are separated by the TNCO. The TNCO is generally considered to be the result of a continent-continent collision between the western NCC (WNCC) and the eastern NCC (ENCC) during the late Paleoproterozoic [e.g., *Zhao et al.*, 2001; *Trap et al.*, 2012]. The eastern part of the NCC subsequently lost its lithospheric root as a result of oceanic subduction of the Paleo-Pacific slab during the Mesozoic [e.g., *Zhu et al.*, 2011]. The ENCC currently has very thin (<100 km) and hot lithosphere [e.g., *He*, 2015], with a mean heat flow of 64 mW/m^2. In contrast with the strong tectonic processes in the east, the WNCC appears to be stable with thick (>180 km) and cold lithosphere [*Chen et al.*, 2014; *He*, 2015], with mean heat flow less than 50 mW/m^2. Locally, there may be some influence from the westward subduction of the Paleo-Pacific slab. The Qilian Orogen, located in the west of the NCC, is a result of Paleozoic collision between the Qaidam Block in the south and the NCC in the north [*Yang et al.*, 2012], which had a complex tectonic evolution with six stages summarized by *Song et al.* [2013] from continental breakup of the Rodinia supercontinent in the Neoproterozoic to continental collision in the Paleozoic. The tectonic setting is presented in Figure 1a.

2. Seismic Daylight Imaging

The principle of seismic daylight imaging (SDI) is based on the concept that the autocorrelation of vertically transmitted waves from sources below a given discontinuity is equivalent to the reflection response for both source and receiver at the same location, including the effects of the free surface [*Claerbout*, 1968]. *Gorbatov et al.* [2013] applied the concept to examine the crustal thickness by constructing *P* reflectivity across Australia. Later, *Kennett* [2015] extended the approach to probe the properties of the lithosphere and asthenosphere across a wide range of geological environments in Australia. All autocorrelograms employed by *Gorbatov et al.* [2013] and *Kennett* [2015] are constructed from continuous waveforms. *Sun and Kennett* [2016a] used just the autocorrelograms for distant earthquake signals with improved efficiency for constructing *P* reflectivity. This is because the teleseismic arrivals isolate the transmitted waves at near-vertical incidence and their free-surface multiples.

2.1. Stacked Autocorrelograms

We select teleseismic events recorded by the dense NCISP stations with signal-to-noise ratio greater than 2.0 for the period between December 2006 and May 2008 . We follow the procedures described in *Sun and Kennett* [2016a] to obtain the stacked autocorrelograms for all broadband stations. Autocorrelograms are extracted for each event recorded by each station after autocorrelating the band-pass-filtered (0.1 – 5 Hz) event waveforms. The *P* reflectivity is constructed from stacking all vertical component autocorrelograms for each of the stations, with a band-pass filter over the frequency band 0.5 – 4 Hz.

Further, the spatial stacking technique of *Kennett et al.* [2015] is employed to enhance the coherence of the reflectivity across the stations. This procedure uses a Gaussian weighting as a function of distance from the master station. Here we use spatial span parameter $\sigma = 0.1°$, so that aperture is limited to 0.3°. This aperture is roughly equal to the Moho depth so that there is comparable resolution in the lateral and vertical directions for the crust, without strongly smoothing structure at depth.

With the aid of the relatively broad band of 0.5 – 4 Hz employed in the SDI method, it is possible to image short-wavelength structures in the lithosphere [*Kennett*, 2015; *Sun and Kennett*, 2016a]. With the dense stations at an average interval of 15 km, we can explore fine-scale lithospheric structure both horizontally and vertically along the profile through the western and central North China Craton.

2.2. Identification of the MLD

The receiver function method employs waveforms with a low and narrow frequency band of 0.03 – 1 Hz for *Ps* and 0.03 – 0.5 Hz for *Sp* [e.g., *Ford et al.*, 2010] with the aim of identifying seismic discontinuities. Interpretation of the nature of the discontinuities can then be made from the positive or negative phase of the receiver function. In contrast, the SDI method employs a higher and broader frequency band of 0.5 – 4 Hz, so that the resulting traces are more complex and interpretation is more difficult without isolated arrivals. Fortunately, variations in frequency character as a function of time (depth) can be used to infer changes within the lithosphere. The frequency change has been applied to identify the Moho discontinuity [*Gorbatov et al.*, 2013; *Kennett et al.*, 2015] and to investigate the lithosphere-asthenosphere transition [*Kennett*, 2015; *Sun and Kennett*, 2016a] across a wide range of geological environments beneath the Australian continent.

Here we show the possibility of interpreting a mid-lithosphere discontinuity from the SDI results using the changes in frequency character on a dense array. The line of stations spans very different geological environments from the Qilian Orogen in the west, across the stable western NCC in the center, to the TNCO and into the eastern NCC with thinned lithosphere. We can therefore examine the performance of the SDI approach for probing the MLD in different lithospheric environments.

In Figure 2, we show results for estimates of *P* reflectivity at six stations located in different tectonic blocks. In the west, stations 372 and 361 are located in the Paleozoic Qilian Orogen. The two stations 355 and 337 in the central group lie on the Archean western NCC, which is stable though locally affected by the westward subduction of Paleo-Pacific slab. In the eastern group, station 321 is in the TNCO arising from Paleoproterozoic collision between the western and eastern NCC, and station 309 lies on the eastern NCC that lost its original lithospheric root in the late Mesozoic. For each station, we show the autocorrelograms for the frequency bands: 0.5 – 4 Hz, 0.05 – 1 Hz, and 1 – 4 Hz. All traces are normalized by the maximum amplitude after applying automatic gain control (AGC) to improve the clarity of later reflections. A detailed description of the AGC method is given in section 1 of Supporting Information S1.

The results for the Moho and the LAB indicated by solid colored lines in Figure 2 are taken from receiver function studies [*Chen*, 2010; *Li et al.*, 2014; *He et al.*, 2014]. For all six stations, as the frequency increases the time behavior of the autocorrelograms becomes more complicated. This is because the influence of fine-scale heterogeneity in physical properties becomes more important at higher frequencies.

We first examine the low-frequency band 0.05 – 1 Hz, similar to that used with *Ps* receiver functions. In general, both the Moho and the LAB indicated by the SDI results (dashed lines in Figure 2) are in good accord with those determined by receiver function. The reflections from the Moho can be observed with significant arrivals in all frequency bands, especially for stations 321 and 309 (see Figures 2e and 2f) lying on the Paleoproterozoic TNCO. Clear arrivals in the neighborhood of the Moho at the other four stations can be also observed in the low-frequency band from 0.05 to 1 Hz (the left trace in Figures 2a – 2d). At higher frequencies such features break up into more complex reflectivity with alternation of positive and negative phases

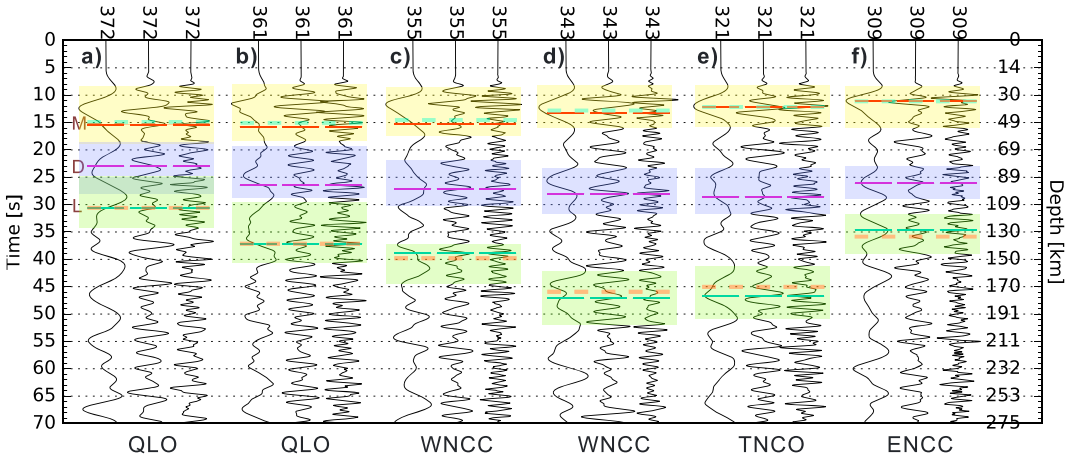

Figure 2. Autocorrelograms for a set of selected stations (see Figure 1b) distributed across different geological environments: (a) 372 and (b) 361 in QLO, (c) 355 and (d) 343 in WNCC, (e) 321 in TNCO, and (f) 309 in ENCC, with ages from Archean to Paleozoic. In each subfigure, three traces are given with different frequency bands of 0.05–1 Hz, 0.5–4 Hz, and 1–4 Hz from left to right. The potential reflections are highlighted with tinted rectangles. The red and cyan short horizontal lines indicate the positions of Moho and LAB determined by receiver function, while the purple lines indicate location of the MLD interpreted by SDI in terms of changes of frequency character. The Moho and LAB interpreted by SDI are also displayed by thick dashed lines. The letters "M," "D," and "L" stand for Moho, MLD, and LAB.

(the center and right traces in Figures 2a–2d). Such complex reflectivity at the base of the crust is often seen in deep seismic reflection profiling. The position of the Moho can thus be determined by tracing the changes of frequency character from the stacked autocorrelograms and matches the receiver function estimates quite well. A similar correspondence is found for the LAB.

In Figure 2, the reflections from Moho show negative polarity for the low-frequency traces, which differ from the positive phase for the conversions in receiver functions. The autocorrelograms are equivalent to the product of the *P* reflectivity from depth and the free-surface reflection coefficients, because the incoming transmitted waves have first to interact with the free surface before being reflected back from depth. Synthetic examples for simple crustal structure [see *Gorbatov et al.*, 2013, Figure 6b] confirm the expectation of negative amplitudes associated with the Moho.

As a result of the strong impedance contrast between the crust and the mantle, reflections later than those from the Moho will be weaker. In Figure 2 we indicate the time intervals that contain the potential reflections from discontinuities by tinted rectangles. We seek the location of the different discontinuities in the SDI results by starting with the low-frequency band (0.05–1 Hz) and adjusting the estimate of the discontinuity time to capture the changes in reflectivity pattern starting with the low-frequency components (0.05–1 Hz) and then bringing in the high-frequency components (0.5–4 Hz and 1–4 Hz). Particularly for the interval around the MLD, we may have multiple potential discontinuity features on the record for a single station. So we exploit the properties of the wavefield across the full dense linear array and select the most spatially continuous feature as the MLD. The detailed procedure for estimating the time to discontinuities is discussed in section 2 of Supporting Information S1.

Compared with receiver functions, the higher frequencies employed by SDI can reveal finer structures in the lithosphere. But the consequence is a visually more cluttered appearance, which can be overcome by tracking variations in frequency content on single records and between stations.

3. *P* Reflectivity Beneath the Western and Central NCC

The SDI approach has been used to construct *P* reflectivity traces up to 70 s two-way time at all stations, with stabilization by weighted spatial stacking linking to neighboring stations. In Figure 3 we display *P* reflectivity for every three stations. The time scale is converted to depth using the *ak*135 model [*Kennett et al.*, 1995]. With the broad span of the profile and the approximately 45 km spacing of the selected stations we can expect to see variations in the character of lithospheric structure from the Paleozoic orogen, across Archean craton, to the Paleoproterozoic orogen (see Figure 1b).

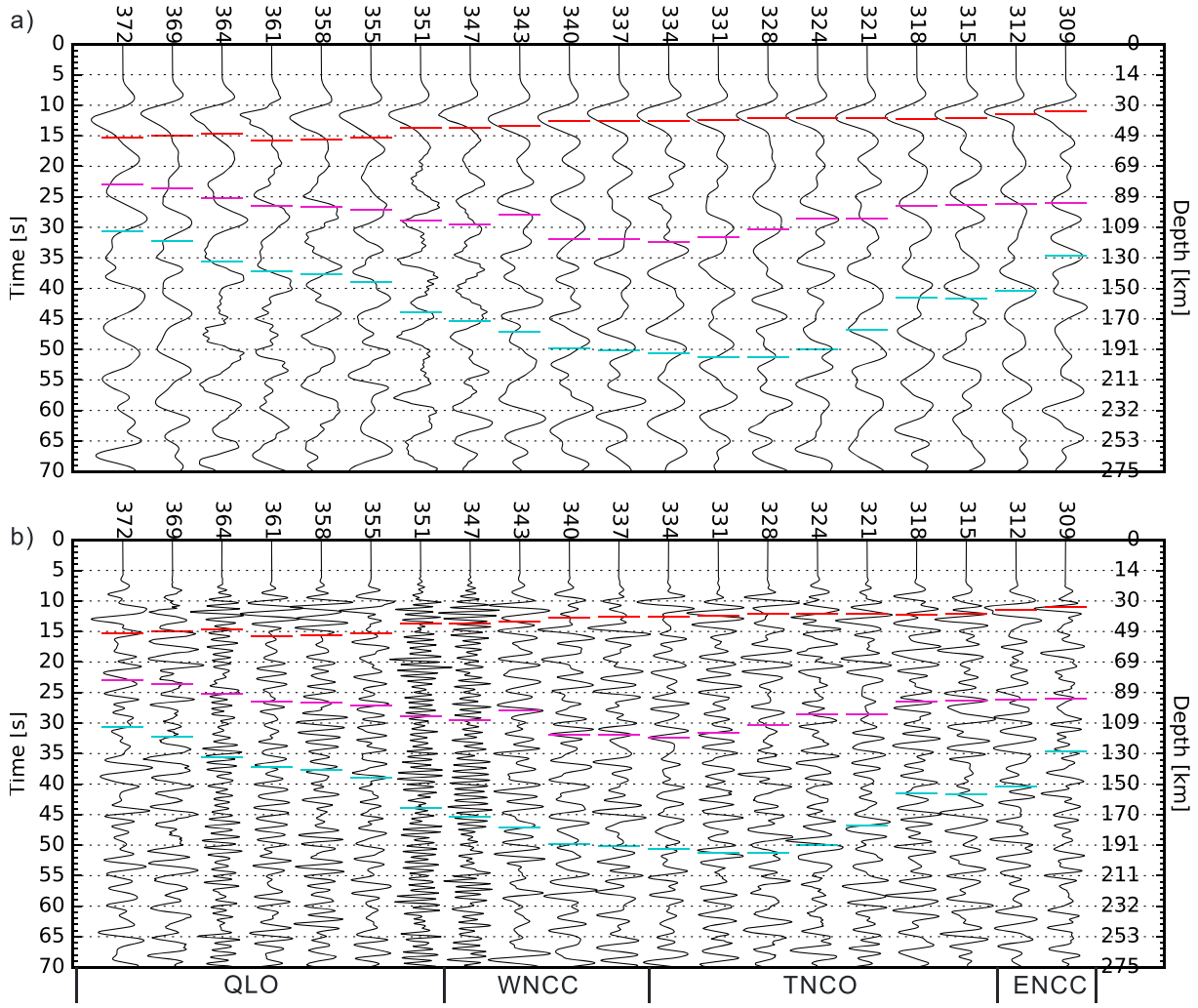

Figure 3. *P* wave reflectivity for the dense stations with different frequency bands of (a) 0.05–1 Hz comparable to receiver function and (b) 0.5–4 Hz revealing finer lithospheric structures. The red markers give the Moho from *Ps* receiver function [*He et al.*, 2014; *Li et al.*, 2014]. The cyan markers indicate the LAB from *Sp* receiver function [*Chen*, 2010]. The MLD denoted by purple markers are interpreted from SDI in this study. Time to depth conversions are made with the *ak*135 model [*Kennett et al.*, 1995]. The geological units are indicated at the base of the figure.

Both the low-frequency (0.05–1 Hz) and high-frequency (0.5–4 Hz) bands are shown in Figures 3a and 3b, so that the changes in reflectivity with frequency are apparent. The traces for the low-frequency band, comparable to receiver functions, allow us to identify long-wavelength seismic discontinuities in the lithosphere, while the high-frequency band can indicate lithospheric structures with wavelength as short as 2 km [*Kennett*, 2015]. Two traces (station 351 and 347) show higher-frequency components in Figure 3b than the other stations, which suggests the presence of strong heterogeneity at the boundary of QLO and WNCC. The *P* reflectivity seen in Figure 3 is complex. The high-frequency results suggest the presence of multiple minor features, though the lower frequency band makes it clear that the feature we have identified as the MLD is the most prominent change in structure with depth below the Moho.

From Figure 3 we see that there is a reasonable correlation of MLD topography with that of the LAB. The depth of the MLD increases from about 83 km beneath the QLO to about 120 km beneath the margin of WNCC and TNCO and then decreases to about 93 km beneath the westernmost part of ENCC. The deep MLD mostly occurs beneath the stable WNCC. The depth range for the MLD (80–120 km) is in good agreement with those reported in other regions.

We make further efforts to examine the MLD beneath the western and central NCC by comparison with a shear wave speed model from surface wave tomography using Rayleigh waves [*Shen et al.*, 2016]. We extract

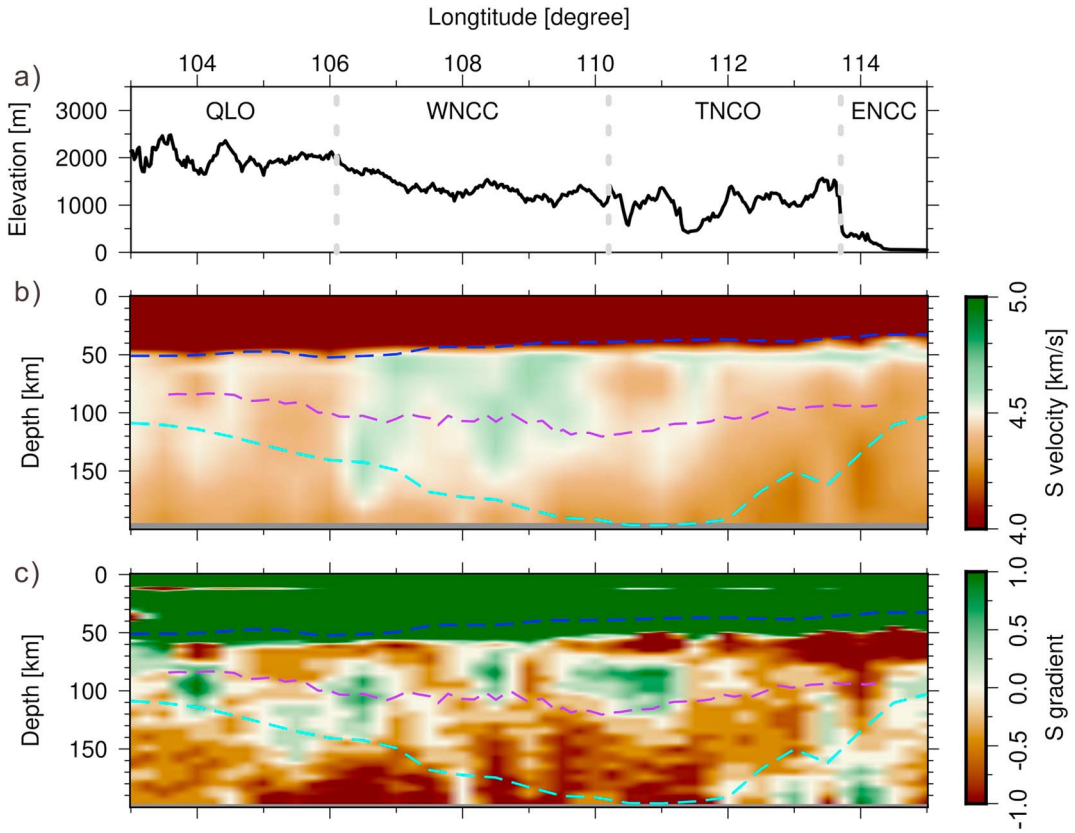

Figure 4. (a) Surface elevation along the Z8 profile decreasing from about 2500 m in the west (QLO) to 42 m in the east (ENCC), (b) shear wave speed along the linear array (approximately 36°N) from Rayleigh wave tomography [*Shen et al.*, 2016], and (c) the gradient of *S* velocity shown in Figure 4b. The Moho and LAB determined by receiver function [*Chen*, 2010; *He et al.*, 2014; *Li et al.*, 2014] are indicated by blue and cyan dashed lines. The MLD marked by purple dashed lines is interpreted from SDI results of all stations shown in Figure 1b.

a vertical section through the wave speed structure along latitude 36°N, which closely follows the line of the 1000 km long station profile. Both ambient noise and earthquake information recorded by all available permanent stations and portable stations in China and adjacent regions have been inverted by *Shen et al.* [2016] to produce this isotropic *S* wave speed model. In Figure 3 we compare the results for the various lithospheric discontinuities from SDI with the tomographic results.

In Figure 4b, a distinctive high *S* velocity beneath WNCC can be seen, which is consistent with the results of *Pn* tomography [e.g., *Sun and Kennett*, 2016b] and teleseismic tomography [e.g., *Zhao et al.*, 2012]. In general, the estimated MLD from the SDI *P* reflectivity matches very well with the location of features in the *S* wave speed, for example, the drop in *S* wave speed in the zone from 107°E to 114°E. This correspondence becomes clearer with a presentation in terms of *S* wave speed gradient (Figure 4c). However, the behavior is not uniform along the profile. Increases in *S* gradient around 104°E and 106.5°E occur in the neighborhood of the MLD, demonstrating strong lateral heterogeneities in the region. The negative *S* gradient beneath the western and central NCC (108°E–113°E) starts at the MLD and continues down to the LAB. In this zone it would appear that the MLD marks the top of a low-velocity zone for *S* waves.

4. Discussion and Conclusions

Our estimated MLD depths are around 80–120 km beneath the western and central NCC, which are reasonably consistent with those (80–100 km) inferred from *Sp* receiver function [*Chen et al.*, 2014]. The SDI approach uses a broader and higher-frequency range 0.5–4 Hz to study the lithosphere, so there is better vertical resolution [*Kennett*, 2015] than the 15 km achievable with *Sp* receiver function for the frequency range 0.05–0.5 Hz [e.g., *Selway et al.*, 2015]. The rather deep MLD is not unique in the western and central NCC. A comparable

MLD depth of 113 km has been reported beneath North America [*Abt et al.*, 2010]. Interestingly, *Calò et al.* [2016] presented at least two MLDs (four at most) beneath North America (see their Figure 7) in the depth range from 75 to 200 km. Our higher-frequency results suggest that the underlying structure shows variations at multiple scales and the characterization in terms of a single discontinuity may be an oversimplification.

The nature of changes in the lithosphere has been investigated for a long time. *Hales* [1969] suggested the presence of a discontinuity at around 80 km depth from analyzing observations from long-range profiles with explosive sources. The concept of the Hales discontinuity was later extended with the "8° discontinuity" [*Thybo and Perchuć*, 1997], again inferred from long-range seismic profiles. Interpretations of *S* velocity decreases at depths around 80–100 km are reported mainly from receiver function [e.g., *Abt et al.*, 2010; *Chen et al.*, 2014; *Ford et al.*, 2010; *Tharimena et al.*, 2016]. However, the Hales discontinuity was initially reported as a *P* velocity increase from 8.0 km/s to around 8.4 km/s at depths of 80–90 km arising from changes of composition. The 8° discontinuity is associated with a reduced *P* wave speed at depths of 90–120 km. The reports of different styles of discontinuities at close depths suggest a complex general feature which we may term an MLD, within the lithospheric mantle.

The existence of the MLD at intermediate depths is reported in tectonically active and stable regions: Australia [*Ford et al.*, 2010; *Kennett*, 2015], North America [*Abt et al.*, 2010; *Calò et al.*, 2016], Ontong Java Plateau [*Tharimena et al.*, 2016], North China Craton [*Chen et al.*, 2014], etc. This would indicate the possibility that mid-lithosphere discontinuities might exist globally [*Karato et al.*, 2015; *Selway et al.*, 2015] but not universally since the MLD cannot be observed in some tectonically active regions with thin lithosphere, e.g., the eastern margin of Australian continent [*Ford et al.*, 2010] and the eastern NCC [*Chen et al.*, 2014].

The mechanism of generation of MLD is still puzzling and cannot be represented by a universal cause. In general, interpretations of the mid-lithosphere discontinuity consider changes of composition, temperature, and anisotropy [e.g., *Karato et al.*, 2015; *Selway et al.*, 2015]. *Karato et al.* [2015] introduced an elastically accommodated grain boundary sliding (EAGBS) model, which could be associated with a thermal induced transition. *Selway et al.* [2015] favor the introduction of hydrated material, specifically amphibole, e.g., through ponding above metasomatism, as a means of locally lowering shear wave speeds. Earlier, *Kennett* [1987] had suggested the need for a change in the character of wave speed heterogeneity in the mid-lithosphere from the character of events at different depth observed at the Warramunga array in northern Australia. The presence of such a change in heterogeneity style can have the appearance of a discontinuity when traversed by lower frequency transmitted waves [*Kennett and Furumura*, 2016]. Often, the distinct feature interpreted as the MLD in receiver function work tends to break up when examined at higher frequency; such a result is a strong indicator for the presence of finer-scale structures.

In many places the MLD may coincide with the onset of a negative gradient in seismic *S* velocity with a low-velocity zone down to the LAB. Strong negative gradients are present beneath WNCC and TNCO (108°E–113°E in Figure 4c). A number of different lines of evidence suggest that the region of the lower lithosphere with steadily diminishing shear wave speed may contain some partial melt. Such a scenario has been proposed for, e.g., North America and Europe by *Thybo* [2006] from *P* wave observations.

Beneath the Ordos Basin *He* [2015] has estimated the thickness of the thermal lithosphere from the crossing of the mantle solidus temperature (1200–1300°C) as around 110 km. This is 80–90 km shallower than seismic lithosphere depth estimates from the zone of elevated shear wave speeds and in close proximity to the location of the MLD in this region. *He* [2015] attributed the disparity between the estimates of the thickness of the thermal and seismological lithospheres to the existence of the rheological transition from a conductive solid lithosphere to convective lithosphere. An extended transition might occur in this region as a result of the thermal influence of Pacific plate subduction beneath the ENCC, in particular the corner flow above the descending plate, that could lead, e.g., to an increase in partial melt in the lower lithosphere beneath the WNCC. In this region, the MLD could thus arise from a thermally induced change of rheology reflected in a modification of the style of fine-scale heterogeneity, with potential anisotropic influences as required by *Wirth and Long* [2014].

In Figure 5 we present a schematic summary of our results across the profile through the North China Craton; the combined thermal and metasomatic influences from Pacific Plate subduction have the effect of shifting

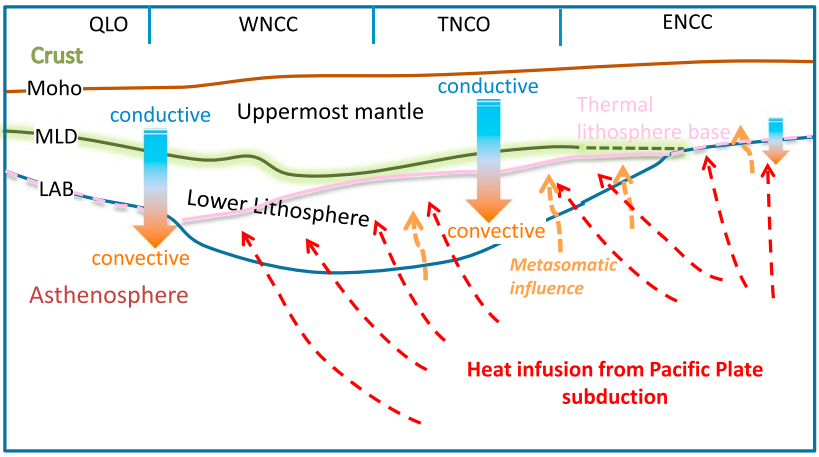

Figure 5. Schematic representation of the relation of the lithospheric discontinuities and the thermal influences. On the eastern side of the North China Craton, the strong heat input from the subduction process and metasomatism shift the base of the thermal lithosphere from close to the seismic LAB to near the MLD that links to the shallow LAB in the far east. The pink line indicates the approximate base of the thermal lithosphere from *Liu et al.* [2016] and is dashed where it coincides with the seismic estimate of the LAB.

the base of the thermal lithosphere away from the seismically determined LAB in the eastern part of the profile, as indicated by the solid pink line. Elsewhere, the thermal lithosphere and the seismic LAB are in close correspondence, indicated by a dashed pink overlay.

The lithosphere displays heterogeneity in physical properties on many scales, and as demonstrated by *Kennett and Furumura* [2016] the interaction of multiples scales of heterogeneity can provide a good representation of a wide range of seismological observations. In such a multiscale heterogeneous environment strong geographic variability is expected in the mid-lithosphere around the transition in styles of heterogeneity, as we see on this detailed profile. The fine-scale MLD observed in the high-frequency traces in Figures 2 and 3 may reflect processes associated with lithosphere thickening or continental formation in the craton region as *Wirth and Long* [2014] suggested for the North American Craton.

Acknowledgments
The research was supported by the National Natural Science Foundation of China (grants 41630210 and 41474105) and the State Key Laboratory of Lithospheric Evolution, Institute of Geology and Geophysics, Chinese Academy of Sciences. The support from Youth Innovation Promotion Association CAS (2017094) is also thanked. The waveform data used in this study were retrieved from the IRIS Data Management Center.

References

Abt, D. L., K. M. Fischer, S. W. French, H. A. Ford, H. Y. Yuan, and B. Romanowicz (2010), North American lithospheric discontinuity structure imaged by Ps and Sp receiver functions, *J. Geophys. Res.*, *115*, B09301, doi:10.1029/2009JB006914.

Calò, M., T. Bodin, and B. Romanowicz (2016), Layered structure in the upper mantle across North America from joint inversion of long and short period seismic data, *Earth Planet. Sci. Lett.*, *449*, 164–175.

Chen, L. (2010), Concordant structural variations from the surface to the base of the upper mantle in the North China Craton and its tectonic implications, *Lithos*, *120*(1–2), 96–115.

Chen, L., M. M. Jiang, J. H. Yang, Z. G. Wei, C. Z. Liu, and Y. Ling (2014), Presence of an intralithospheric discontinuity in the central and western North China Craton: Implications for destruction of the craton, *Geology*, *42*(3), 223–226.

Claerbout, J. F. (1968), Synthesis of a layered medium from its acoustic transmission response, *Geophysics*, *33*(2), 264–269.

Ford, H. A., K. M. Fischer, D. L. Abt, C. A. Rychert, and L. T. Elkins-Tanton (2010), The lithosphere-asthenosphere boundary and cratonic lithospheric layering beneath Australia from *Sp* wave imaging, *Earth Planet. Sci. Lett.*, *300*(3–4), 299–310.

Gorbatov, A., E. Saygin, and B. L. N. Kennett (2013), Crustal properties from seismic station autocorrelograms, *Geophys. J. Int.*, *192*(2), 861–870.

Hales, A. L. (1969), A seismic discontinuity in the lithosphere, *Earth Planet. Sci. Lett.*, *7*, 44–46.

He, R. Z., X. F. Shang, C. Q. Yu, H. J. Zhang, and R. D. Van der Hilst (2014), A unified map of Moho depth and *V-p/V-s* ratio of continental China by receiver function analysis, *Geophys. J. Int.*, *199*(3), 1910–1918.

He, L. J. (2015), Thermal regime of the North China Craton: Implications for craton destruction, *Earth Sci. Rev.*, *140*, 14–26.

Karato, S. I., T. Olugboji, and J. Park (2015), Mechanisms and geologic significance of the mid-lithosphere discontinuity in the continents, *Nat. Geosci.*, *8*(7), 509–514.

Kennett, B. L. N. (1987), Observational and theoretical constraints on crustal and upper mantle heterogeneity, *Phys. Earth Planet. Inter.*, *47*, 319–332.

Kennett, B. L. N. (2015), Lithosphere-asthenosphere *P*-wave reflectivity across Australia, *Earth Planet. Sci. Lett*, *431*, 225–235.

Kennett, B. L. N., and T. Furumura (2016), Multiscale seismic heterogeneity in the continental lithosphere, *Geochem. Geophys. Geosyst.*, *17*, 791–809, doi:10.1002/2015GC006200.

Kennett, B. L. N., E. R. Engdahl, and R. Buland (1995), Constraints on seismic velocities in the Earth from traveltimes, *Geophys. J. Int.*, *122*(1), 108–124.

Kennett, B. L. N., E. Saygin, and M. Salmon (2015), Stacking autocorrelograms to map Moho depth with high spatial resolution in southeastern Australia, *Geophys. Res. Lett.*, *42*(18), 7490–7497, doi:10.1002/2015GL065345.

Li, Y. H., M. T. Gao, and Q. J. Wu (2014), Crustal thickness map of the Chinese mainland from teleseismic receiver functions, *Tectonophysics*, *611*, 51–60.
Liu, Q. Y., L. Y. Zhang, C. Zhang, and L. J. He (2016), Lithospheric thermal structure of the North China Craton and its geodynamic implications, *J. Geodyn.*, *102*, 139–150, doi:10.1016/j.jog.2016.09.005.
Song, S. G., Y. L. Niu, L. Su, and X. H. Xia (2013), Tectonics of the North Qilian orogen, NW China, *Gondwana Res.*, *23*(4), 1378–1401.
Selway, K., H. Ford, and P. Kelemen (2015), The seismic mid-lithosphere discontinuity, *Earth Planet. Sci. Lett.*, *414*, 45–57.
Shen, W. S., M. H. Ritzwoller, D. Kang, Y. Kim, F. C. Lin, J. Y. Ning, W. T. Wang, Y. Zheng, and L. Q. Zhou (2016), A seismic reference model for the crust and uppermost mantle beneath China from surface wave dispersion, *Geophys. J. Int.*, *206*(2), 954–979.
Sun, W. J., and B. L. N. Kennett (2016a), Receiver structure from teleseisms: Autocorrelation and cross correlation, *Geophys. Res. Lett.*, *43*(12), 6234–6242, doi:10.1002/2016GL069564.
Sun, W. J., and B. L. N. Kennett (2016b), Uppermost mantle *P* wavespeed structure beneath eastern China and its surroundings, *Tectonophysics*, *683*, 12–26, doi:10.1016/j.tecto.2016.06.011.
Tharimena, S., C. A. Rychert, and N. Harmon (2016), Seismic imaging of a mid-lithospheric discontinuity beneath Ontong Java Plateau, *Earth Planet. Sci. Lett.*, *450*, 62–70.
Trap, P., M. Faure, W. Lin, N. Le Breton, and P. Monie (2012), Paleoproterozoic tectonic evolution of the Trans-North China Orogen: Toward a comprehensive model, *Precambrian Res.*, *222*, 191–211.
Thybo, H. (2006), The heterogeneous upper mantle low velocity zone, *Tectonophysics*, *416*, 53–79.
Thybo, H., and E. Perchuć (1997), The seismic 8° discontinuity and partial melting in continental mantle, *Science*, *275*(5306), 1626–1629.
Wirth, E. A., and M. D. Long (2014), A contrast in anisotropy across mid-lithospheric discontinuities beneath the central United States—A relic of craton formation, *Geology*, *42*, 851–854.
Yang, J. H., Y. S. Du, P. A. Cawood, and Y. J. Xu (2012), From subduction to collision in the northern Tibetan Plateau: Evidence from the Early Silurian clastic rocks, northwestern China, *J. Geol.*, *120*(1), 49–67.
Zhao, G. C., S. A. Wilde, P. A. Cawood, and M. Sun (2001), Archean blocks and their boundaries in the North China Craton: Lithological, geochemical, structural and *P-T* path constraints and tectonic evolution, *Precambrian Res.*, *107*(1–2), 45–73.
Zhao, L., R. M. Allen, T. Zheng, and R. Zhu (2012), High-resolution body wave tomography models of the upper mantle beneath eastern China and the adjacent areas, *Geochem. Geophy. Geosys.*, *13*(6), Q06007, doi:10.1029/2012GC004119.
Zhu, R. X., L. Chen, F. Y. Wu, and J. L. Liu (2011), Timing, scale and mechanism of the destruction of the North China Craton, *Sci. China Earth Sci.*, *54*(6), 789–797.